Electronic Supplementary Material (ESI) for Journal of Materials Chemistry C.

Chemically Robust Amine-grafted Zn(II)-based Smart Supramolecular gel as a Regenerative Platform for Trace Discrimination of Nitro-antibiotics and Assorted Environmental Toxins

Ekata Saha,[a,b] Ashis Chhetri,[a,b,c] Pushyaraga P. Venugopal,[d] Debashree Chakraborty, [d] Joyee Mitra[a,b] *

[a] Inorganic Materials & Catalysis (IMC) Division, CSIR-Central Salt & Marine Chemicals Research Institute, Gijubhai Badheka Marg, Bhavnagar-364002, Gujarat, India.

[b] Academy of Scientific and Innovative Research (AcSIR), AcSIR Headquarters, CSIR-HRDC Campus, Ghaziabad-201002, U.P., India.

[c] School of Science, RMIT University, Melbourne, Vic 3000, Australia.

[d] Biophysical and Computational Chemistry Laboratory, Department of Chemistry, National Institute of Technology Karnataka, Surathkal, Mangalore, India - 575025

E-mail: joyeemitra@csmcri.res.in, joyeemitra@gmail.com

Figures: 34 (S1 – S34)

Tables: 7 (S1 – S7)

Pages: 33 (S1 – S33)

Index

Experimental Details

All reagents and solvents for synthesis and analyses were commercially available and used as received without further purification. N, N-Dimethylformamide (DMF) purchased from Finar. Zinc(II) acetate tetrahydrate [$Zn(OAc)_2.4H_2O$], Hydrochloric acid (HCl), Sodium Hydroxide pellets, Ammonia solution, Ammonium thiocyanate, Glacial Acetic acid, Ethylenediaminetetraacetic acid (EDTA) were procured from Fisher Scientific (SQ grade, Qualigens), Rankem (LR grade), Merck, Qualigens (SQ grade), Fisher Scientific (Certified ACS grade), Fisher scientific (SQ grade, Qualigens) and SD Fine Chemicals (AR grade) respectively. Triphenylphosphine, Tetra-butyl Ammonium bromide, Silver nitrate, Lithium fluoride, Sodium chloride, Potassium bromide, Potassium iodide and picric acid were purchased from Loba Chemie, Spectrochem, Qualigens, SD Fine Chemicals, Fisher scientific, SD Fine Chemicals, Qualikems and Loba Chemie respectively. 2,4-dinitrotoluene, 4-nitrotoluene, 3-nitrotoluene, 2-nitrotoluene, 2,4-dinitrophenol, 3-nitrophenol, 2-nitrophenol and 4-nitrophenol were procured from TCI Chemicals. 3,5-diammino-1,2,4-traizole, 3-nitrobenzoic acid and *p*-nitrobenzoic acid were obtained from Sigma Aldrich and used as received. Furazolidone, nitrofurantoin, ornidazole, secnidazole and tinidazole were obtained from reliable commercial sources and were used without further purifications.

Instrument Details

The synthesized metallogel and corresponding xerogel were characterized using several techniques such as PXRD, FT-IR, UV-vis, Emission analysis, TEM, SEM and dynamic rheological studies. The powder X-ray diffraction (PXRD) analysis was done using Philips X'pert MPD system (PANalytical diffractometer) with Cu $K\alpha_1$ radiation (λ = 0.15406 nm). The diffraction pattern was measured from 5-90° 2θ range at operating voltage of 40 kV and 30 mA current, with a scan speed of 3º min^{-1} and a step size of 0.013º in 2θ at RT with a scan step time 58.395 sec. Anode Material was Cu and the value of $K_{\alpha1}$, $K_{\alpha2}$ and K_{β} were 1.54060

[Å], 1.54443 [Å] and 1.39225 [Å] respectively. $K_{\alpha2}/K_{\alpha1}$ Ratio was 0.50000. Fourier transform Infrared Spectra analysis (FT-IR) was recorded on Perkin Elmer-Spectrum G-FTIR spectrometer (Germany) from 400-4000 cm^{-1} with a resolution of 4 cm^{-1} using KBr pellets. The UV-visible (UV-vis) spectra and emission spectra of samples were recorded using UV 3600, Shimadzu (Japan) and Fluorolog Horiba Jobin fluorometer respectively. The slit-width for the fluorescence experiment was kept at 5 nm (excitation) and 5 nm (emission) and the excitation wavelength was set at 275 nm. The surface morphology of prepared gel material was analyzed by Field Emission-Scanning Electron Microscope JEOL JSM 7100F (using accelerating voltage of 5–15 kV with 10 μA of emission current) and by transition electron microscope (TEM) JEOL, JEM 2100. LEICA EM ACE200 sputter coater was used for gold coating of the samples before analyzed under the Field Emission-Scanning Electron Microscope. The exact mass analyses of samples were analyzed by LC-MS analysis (LC Waters, MS Micromass). The rheological properties of samples were measured by the Anton Paar Rheometer with a plate probe of 40 nm diameter. For the amplitude sweep experiment (Dynamic strain sweep, DSS) and thixotropic loop test, the operating frequency was kept constant at 1 rad s^{-1}. For the dynamic frequency sweep measurements, the operating strain was kept constant at 0.1% over the entire frequency range.

Details of the Density functional theory calculations

The 3D structures for nitroaromatics and nitro-antibiotics were generated using the builder panel in Maestro GUI. The geometry of NACs and NDs are then optimized by semi-empirical PM3 [1] using Gaussian09 package [2]. The optimized interaction of Nit/4-NP@ZnGel is proposed using B3LYP functional [3,4] and 6-311++G(d,p) basis set[5]. The energy values corresponding to highest occupied molecular orbital (HOMO) and lowest unoccupied molecular orbital (LUMO) were obtained from this quantum chemical calculations. The HOMO-LUMO energy gap value predicts the chemical reactivity of the molecules. The

distribution of HOMO-LUMO orbitals were generated using Cubegen utility in Gaussian09 software.

Analytical data

ZnGel: FT-IR (KBr) ν_{max}(cm^{-1}): 3471 (m, br), 3072 (w), 2932 (m), 2872 (w), 2593 (w), 2515 (w), 2337 (w), 2274 (w), 2181 (w), 2119 (w), 2051 (w), 1965 (w), 1671 (s), 1498 (m), 1438 (w), 1390 (s), 1252 (s), 1097 (s), 868 (m), 762 (w), 666 (s), 616 (w), 408 (m).

ZnXero: FT-IR (KBr) ν(cm^{-1}): 3376 (m,br), 2936 (w), 1671 (m), 1589 (s), 1539 (w), 1519 (w), 1408 (m), 1389 (w), 1338 (m), 1103 (w), 1069 (w), 1022 (w), 936 (w), 850 (w), 764 (m), 681 (m), 623 (w), 562 (w), 505 (w), 412 (m).

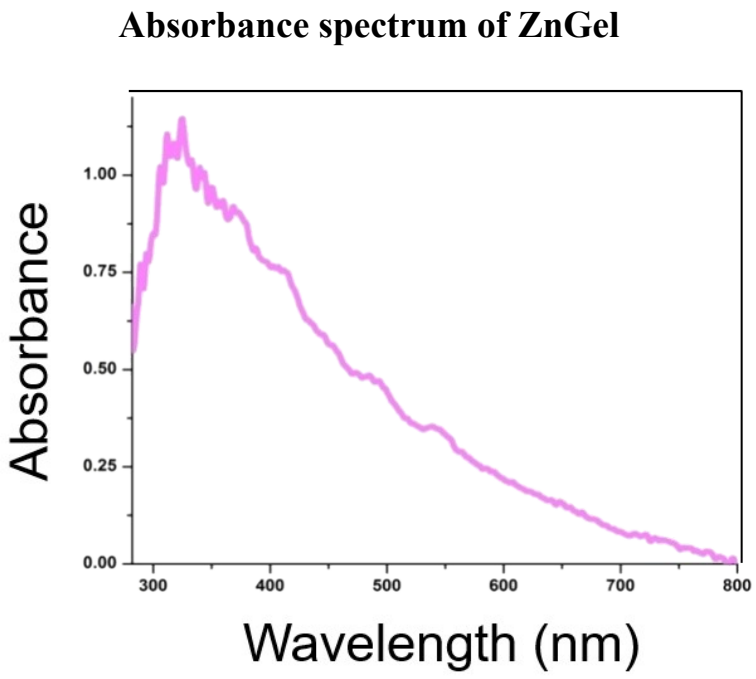

Figure S1. Absorbance spectrum of **ZnGel**.

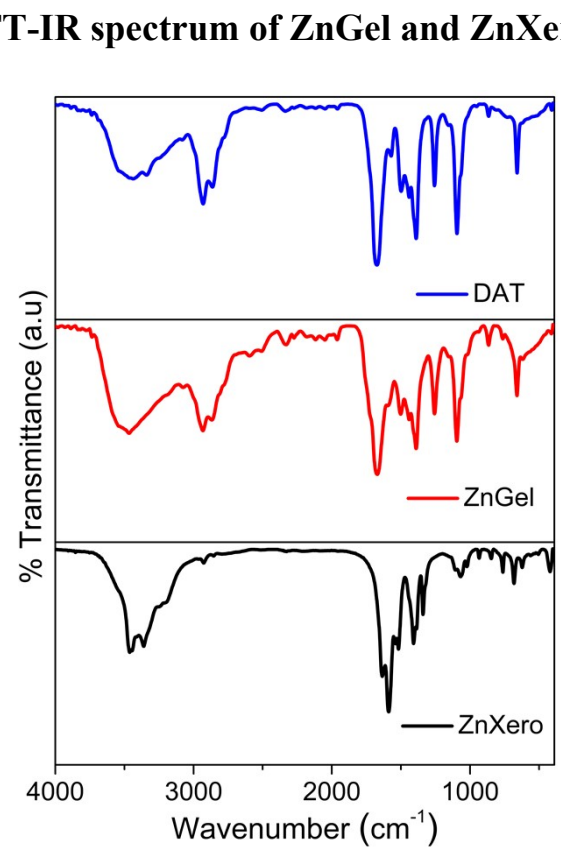

Figure S2. FT-IR spectrum of DAT, **ZnGel** and **ZnXero**.

PXRD pattern of the ZnGel and ZnXero

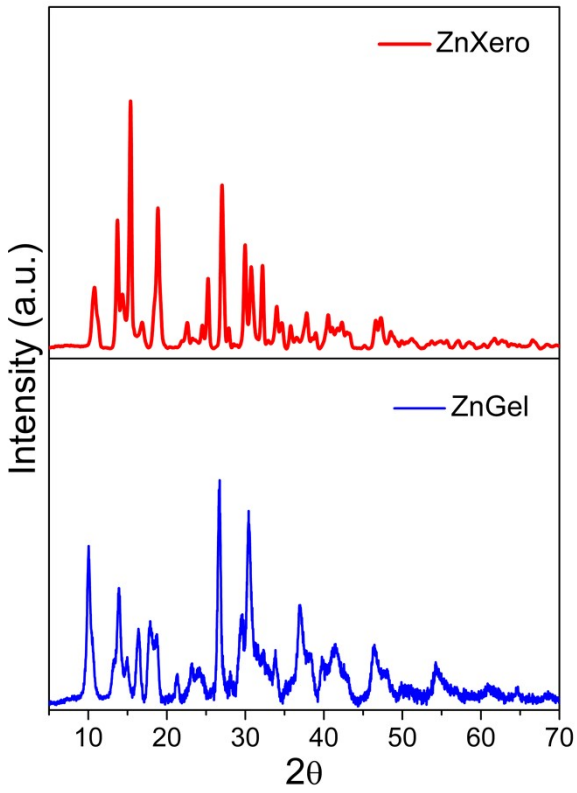

Figure S3. PXRD pattern of the **ZnGel** and **ZnXero**.

Mass spectrum of ZnGel

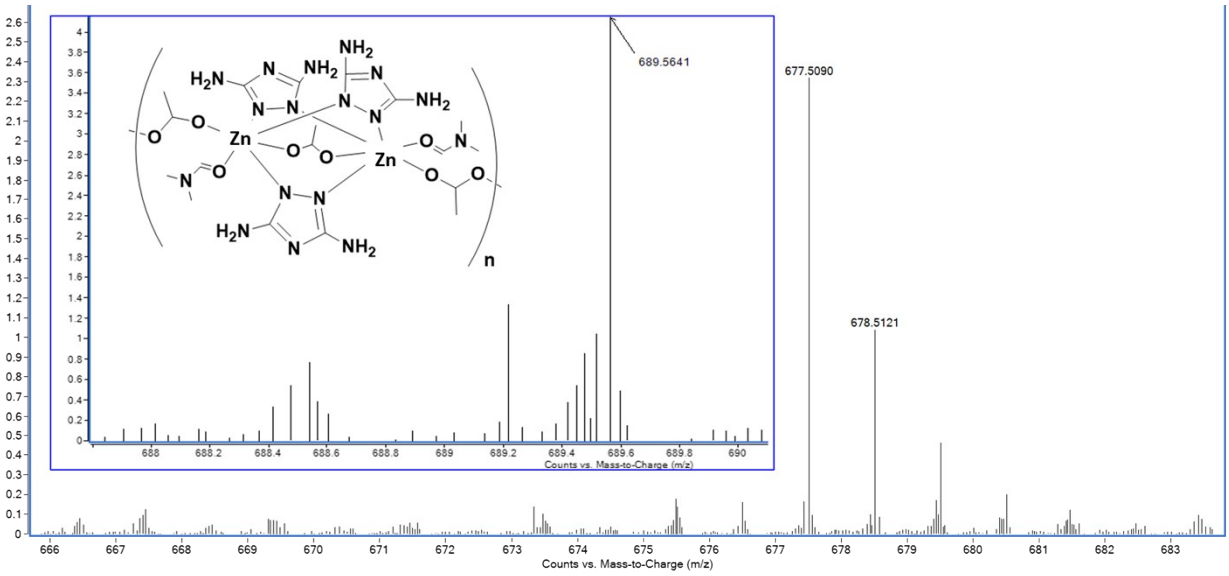

Figure S4. Mass spectrum of **ZnGel** (inset: the local structure of **ZnGel** and the corresponding molecular ion peak at m/z = 689.56).

SEM images (including EDX analysis) of ZnGel and analyte incorporated ZnGel

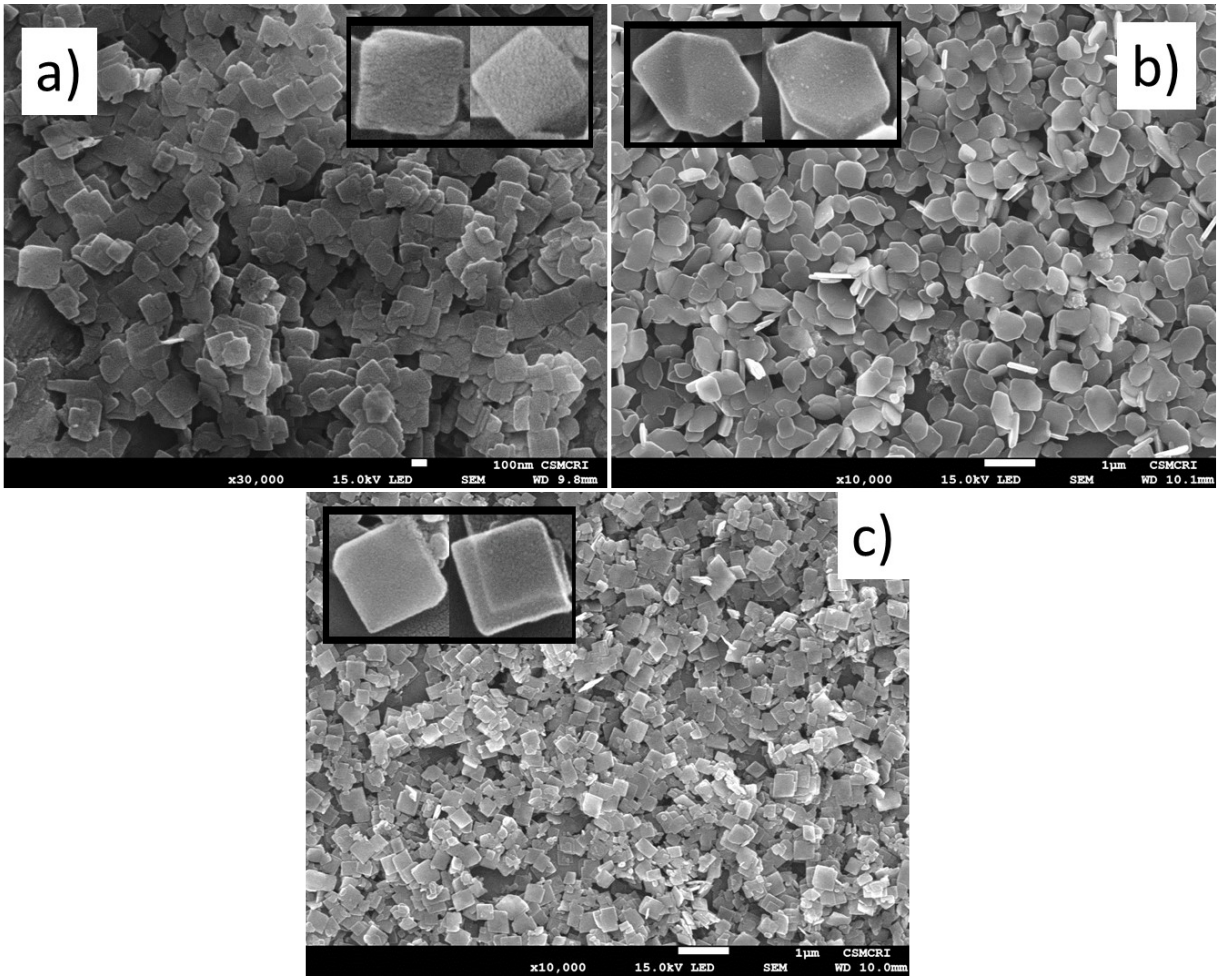

Figure S5. FE-SEM images of a) **ZnGel**, b) PA@**ZnGel**, and c) Nit@**ZnGel** respectively.

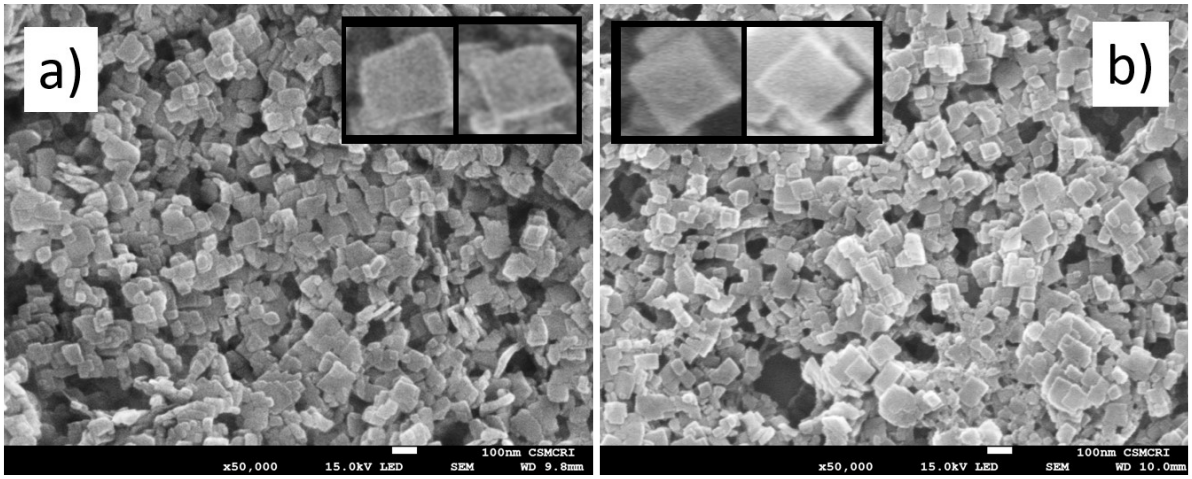

Figure S6. FE-SEM images of a) Fe(III)@**ZnGel** and b) Pd(II)@**ZnGel** respectively.

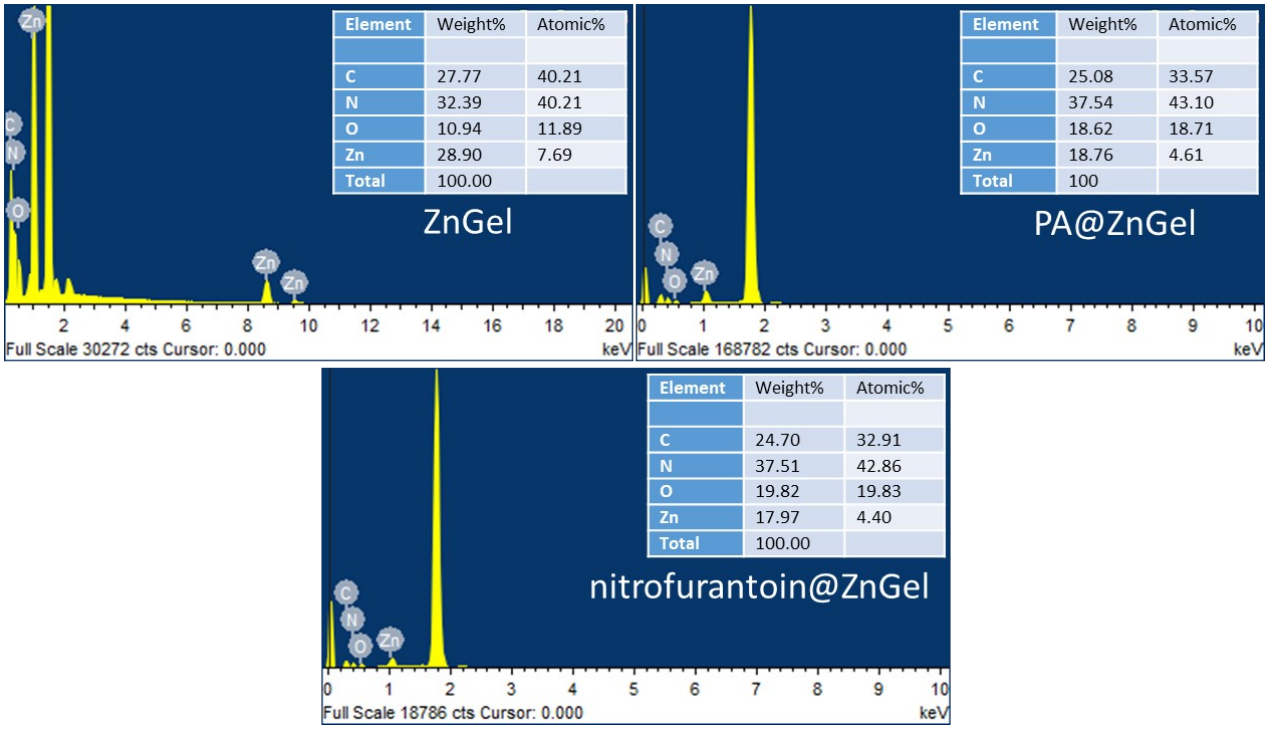

Figure S7. FE-SEM EDX analysis of a) **ZnGel**, b) PA@**ZnGel**, and c) Nit@**ZnGel** respectively.

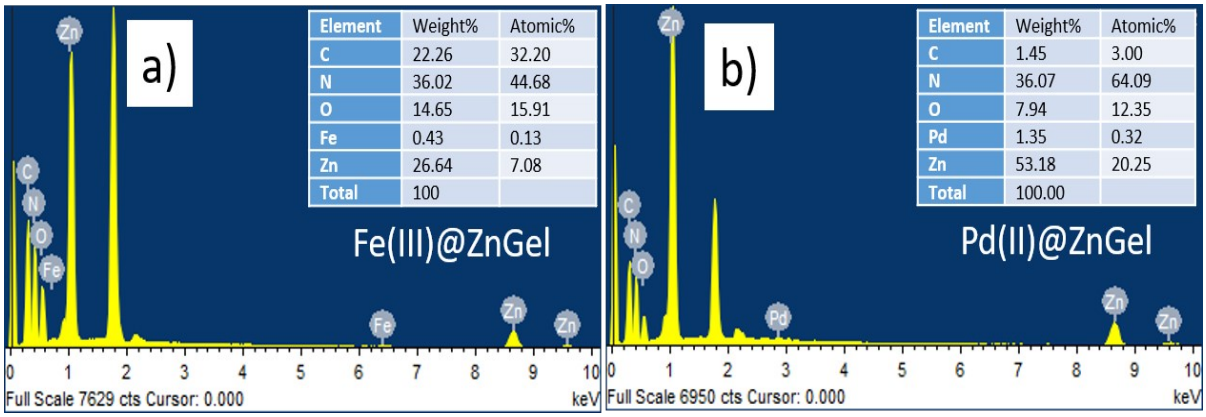

Figure S8. FE-SEM EDX analysis of a) Fe(III)@**ZnGel** and b) Pd(II)@**ZnGel** respectively.

TEM images (including EDX analysis) of ZnGel and analyte incorporated ZnGel

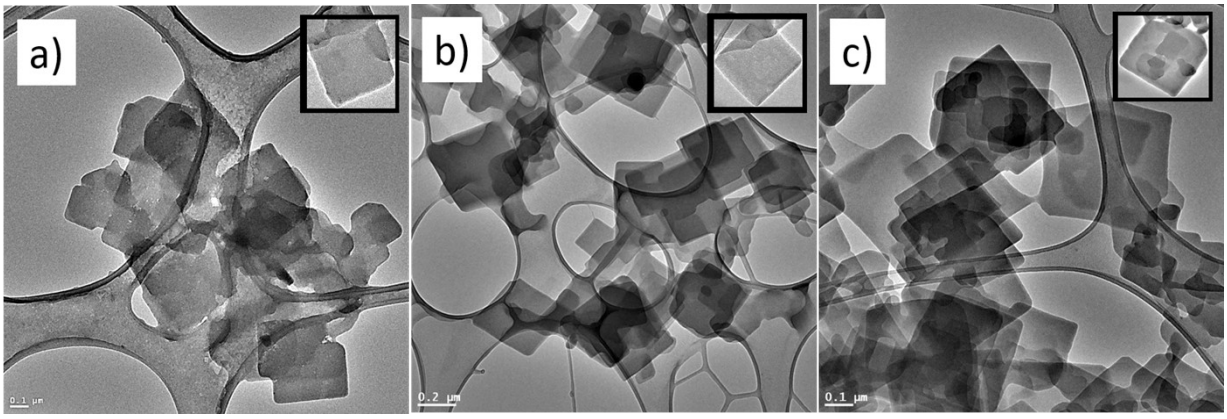

Figure S9. TEM images of a) **ZnGel**, b) Nit@**ZnGel** and c) Furz@**ZnGel** respectively.

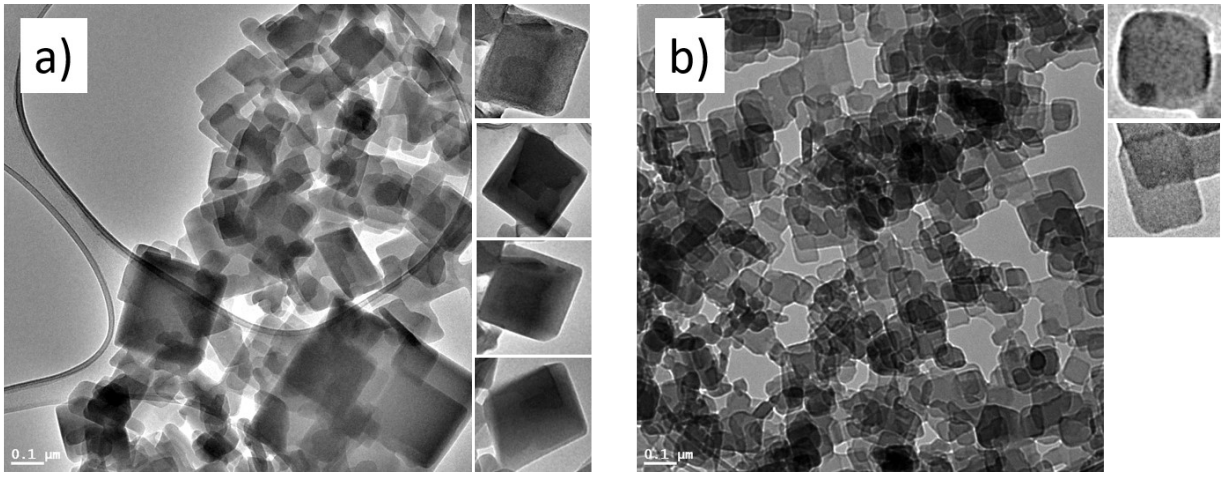

Figure S10. TEM images of a) PA@**ZnGel** and b) Fe(III)@**ZnGel** respectively.

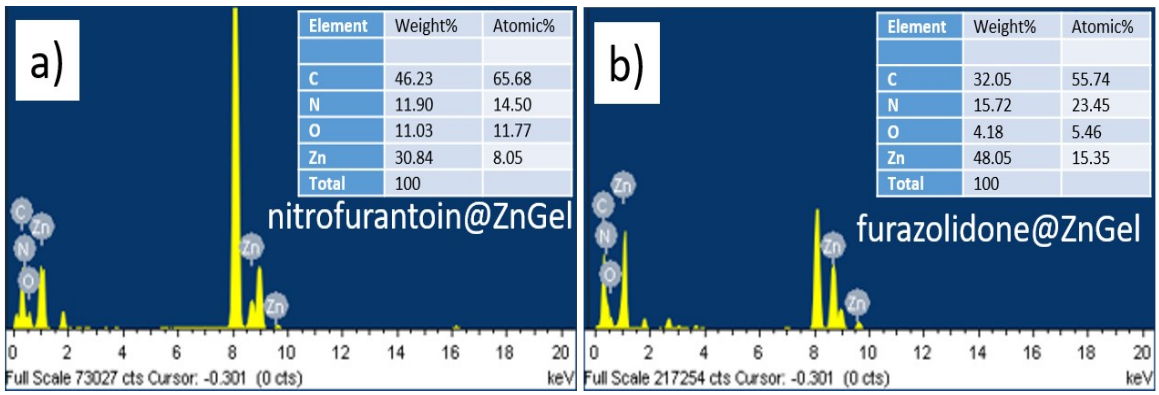

Figure S11. TEM EDX analysis of a) Nit@**ZnGel** and b) Furz@**ZnGel** respectively.

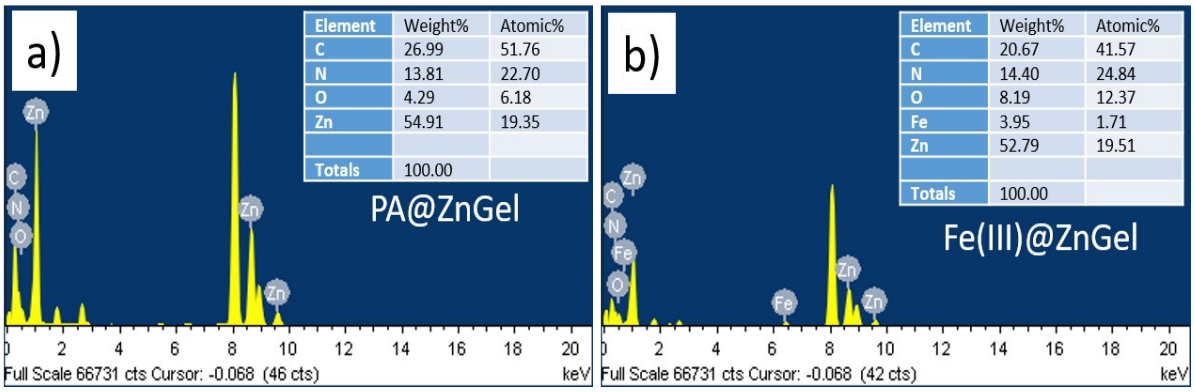

Figure S12. TEM EDX analysis of a) PA@**ZnGel** and b) Fe(III)@**ZnGel** respectively.

Injectable nature of ZnGel

Figure S13. Injectable nature of **ZnGel**.

Response of ZnGel towards treatment with PPh_3 and with external halide stimuli

Figure S14. Response (i.e. irreversible *gel-to-sol* transformation of **ZnGel** a) towards treatment with PPh_3 followed by Zn^{II}-precursor; b) upon addition of external halide stimuli.

Fluorescence titration of ZnGel in DMF in presence of different NDs

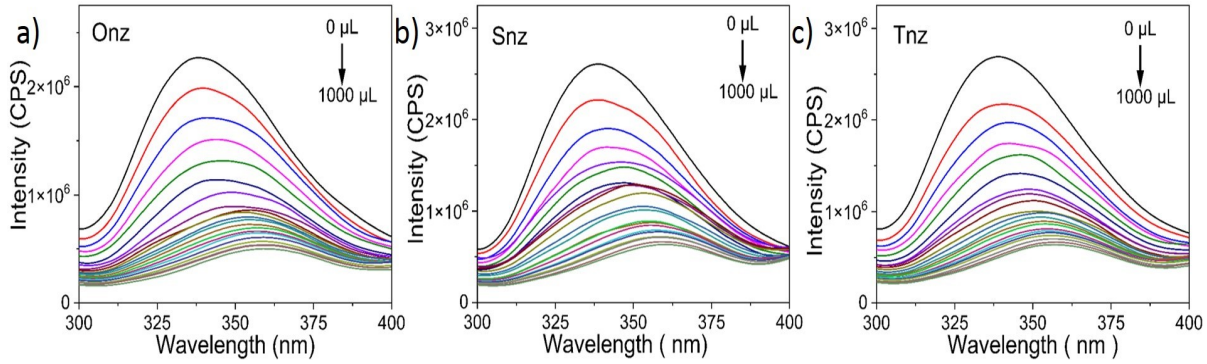

Figure S15. Fluorescence titrations of **ZnGel** in DMF (λ_{ex} = 275 nm) with a) Onz, b) Snz and c) Tnz respectively.

Stern-Volmer plots of ZnGel in DMF in presence of different NDs

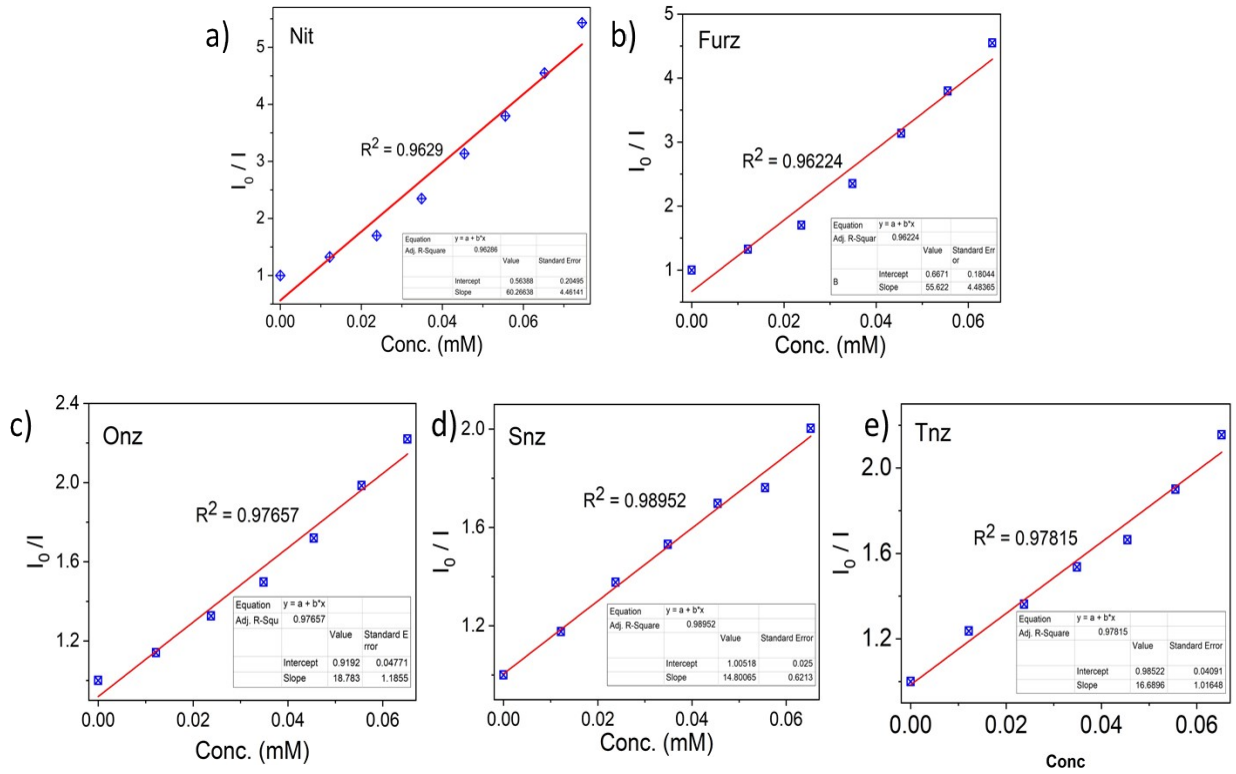

Figure S16. Stern-Volmer plots of **ZnGel** in DMF (λ_{ex} = 275 nm) with a) Nit, b) Furz, c) Onz, d) Snz and e) Tnz respectively.

Intensity of ZnGel vs concentration of the NDs plot

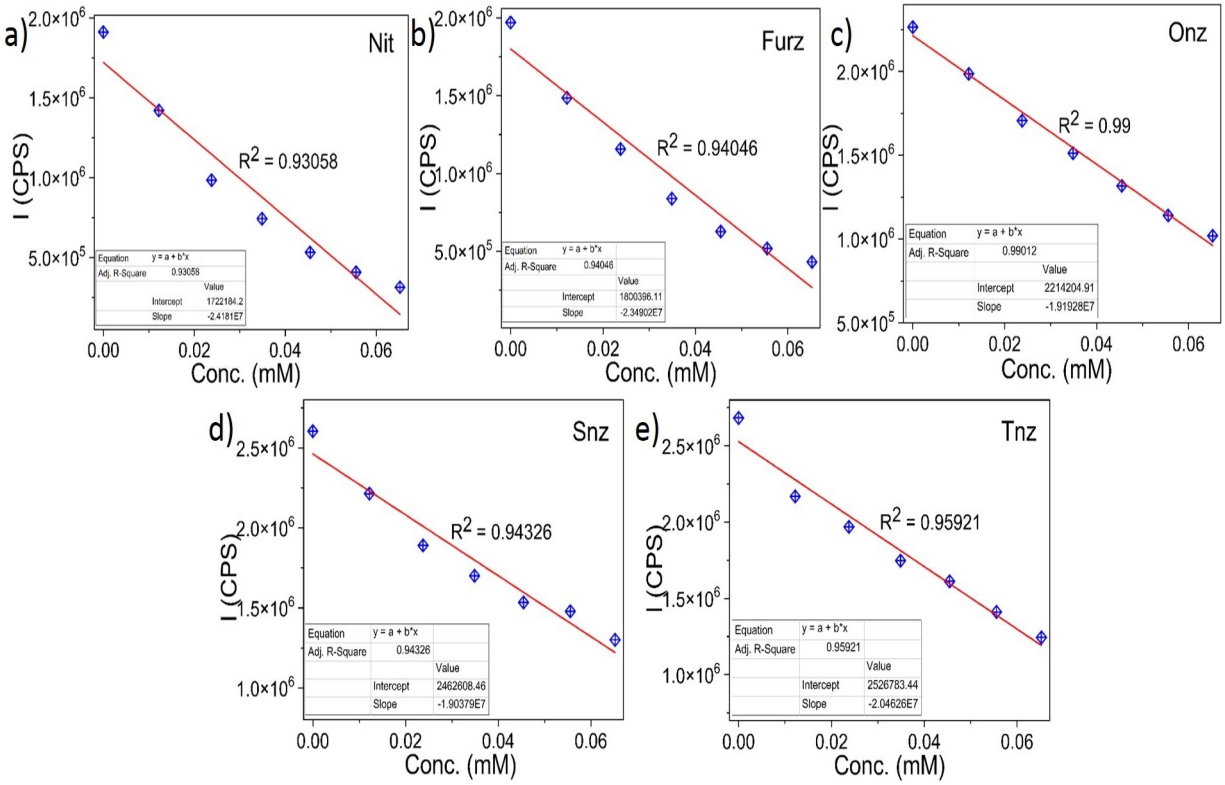

Figure S17. C vs I plots of **ZnGel** in DMF (λ_{ex} = 275 nm) with a) Nit, b) Furz, c) Onz, d) Snz and e) Tnz respectively.

Fluorescence titrations of ZnGel in DMF in presence of different NACs

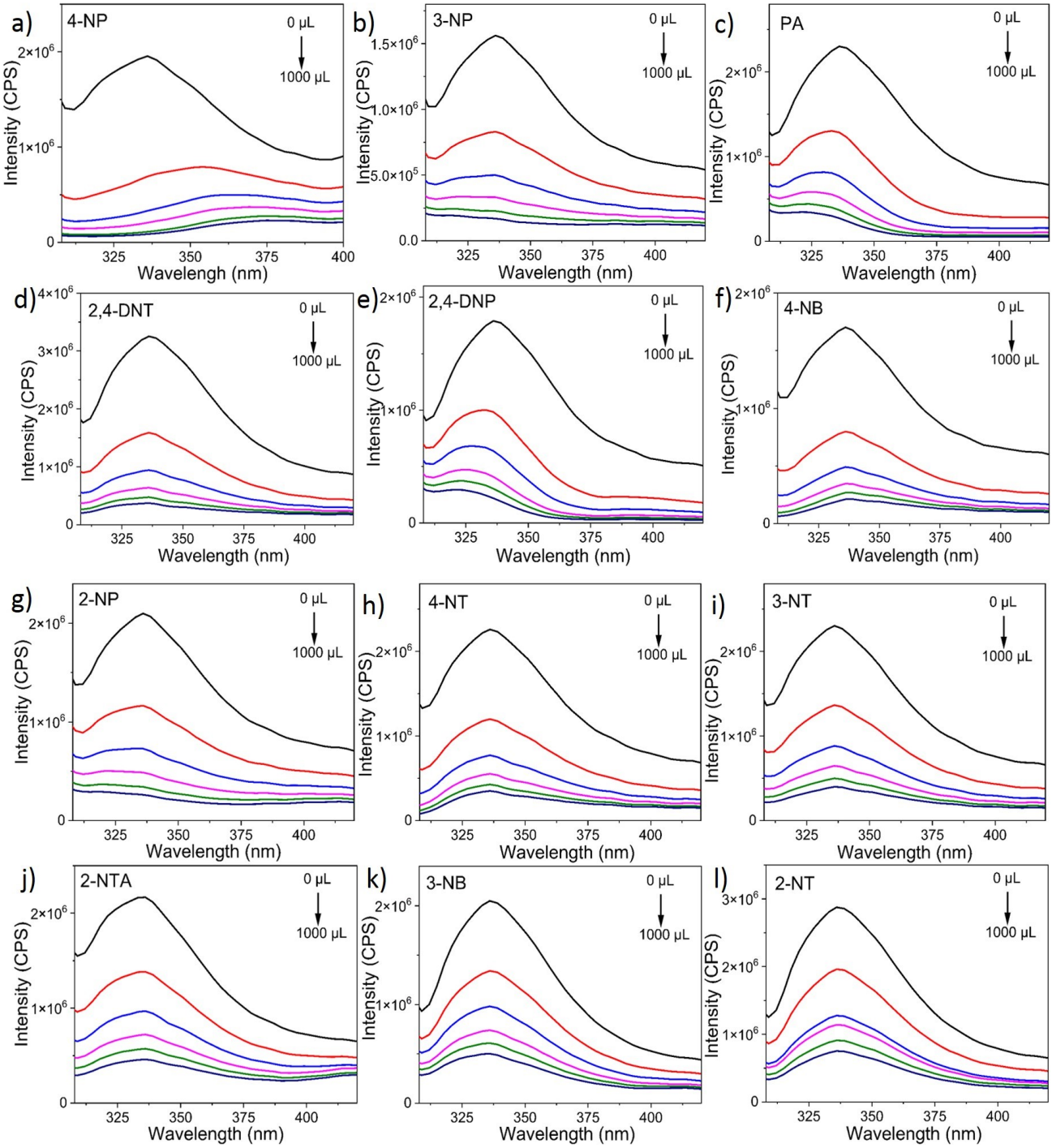

Figure S18. Fluorescence titrations of **ZnGel** in DMF (λ_{ex} = 275 nm) with a) 4-NP; b) 3-NP; c) PA; d) 2,4-DNT; e) 2,4-DNP; f) 4-NB; g) 2-NP; h) 4-NT; i) 3-NT; j) 2-NTA; k) 3-NB; and l) 2-NT respectively.

Stern-Volver plots of ZnGel in DMF in presence of different NACs

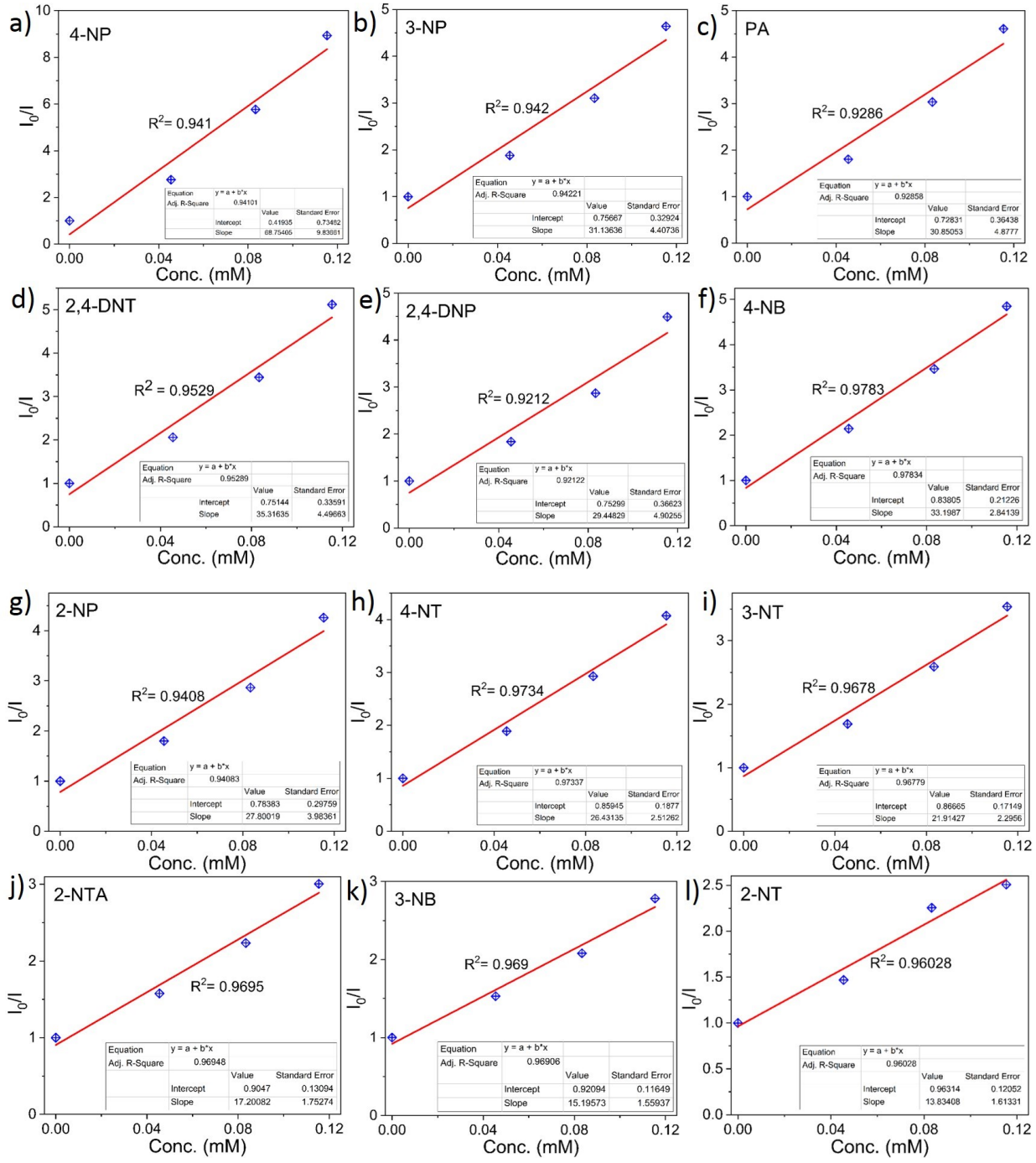

Figure S19. Stern-Volmer plots of **ZnGel** in DMF (λ_{ex} = 275 nm) with a) 4-NP; b) 3-NP; c) PA; d) 2,4-DNT; e) 2,4-DNP; f) 4-NB; g) 2-NP; h) 4-NT; i) 3-NT; j) 2-NTA; k) 3-NB; and l) 2-NT respectively.

Intensity of ZnGel vs concentration of the NACs plot

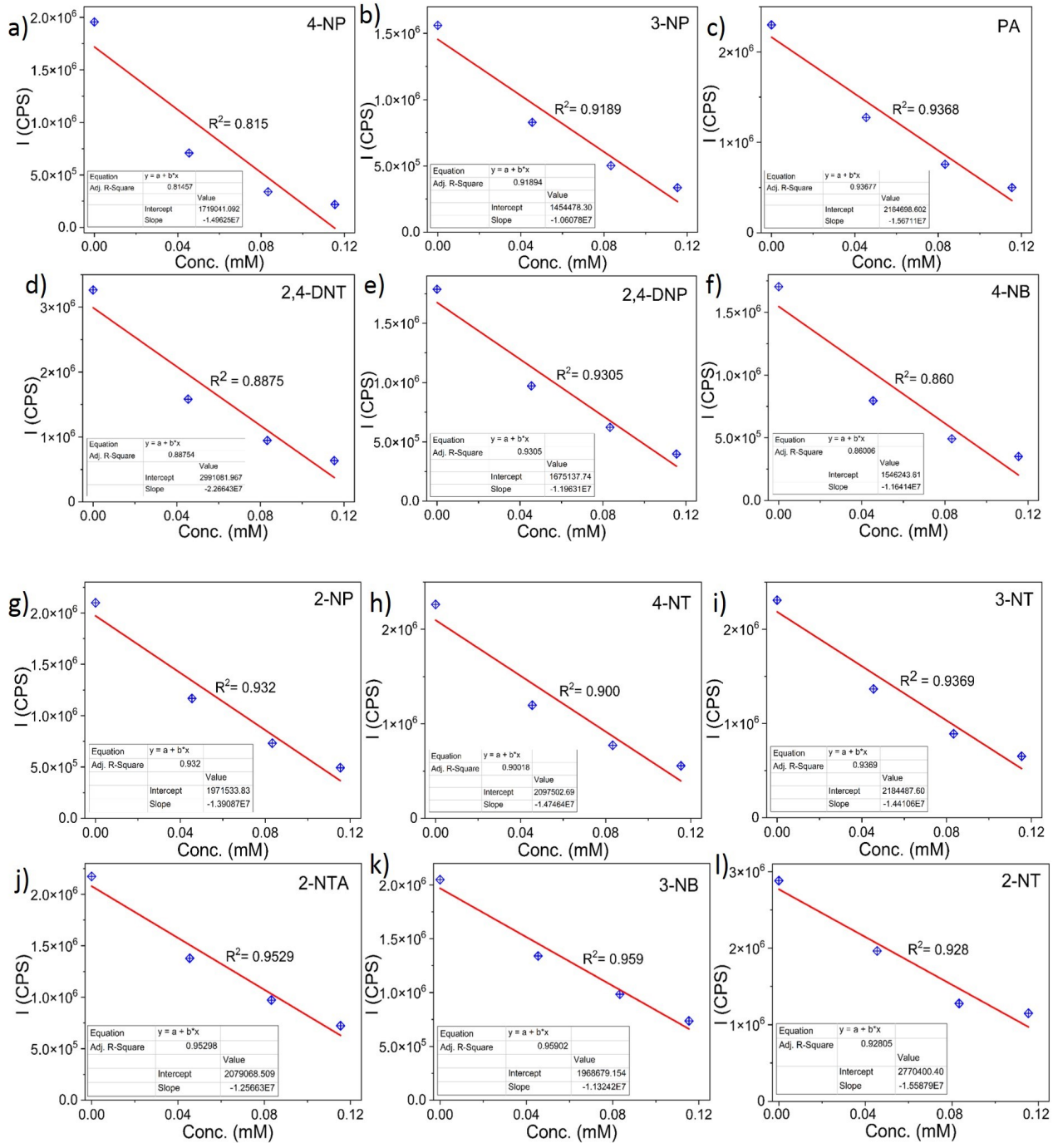

Figure S20. C vs I plots of **ZnGel** in DMF (λ_{ex} = 275 nm) with a) 4-NP; b) 3-NP; c) PA; d) 2,4-DNT; e) 2,4-DNP; f) 4-NB; g) 2-NP; h) 4-NT; i) 3-NT; j) 2-NTA; k) 3-NB; and l) 2-NT respectively.

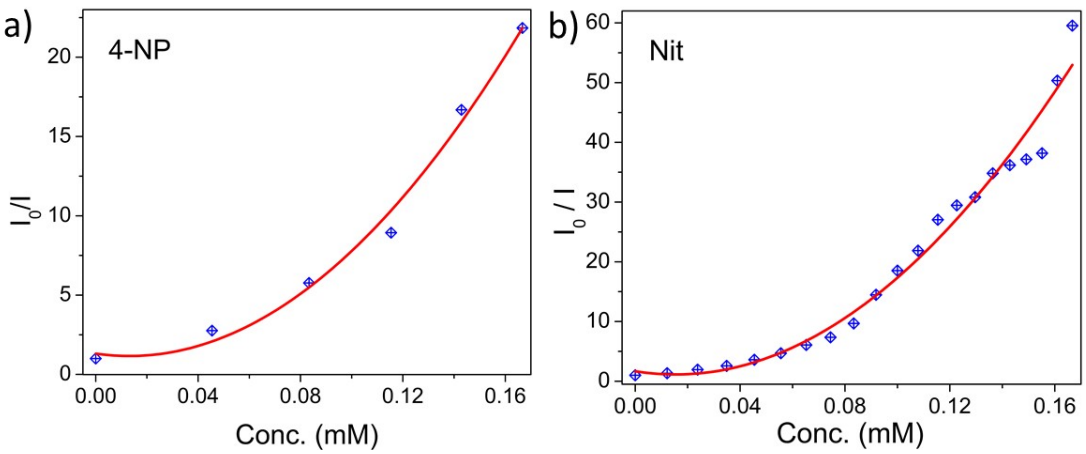

Figure S21. The non-linear Stern-Volmer plot of **ZnGel** in DMF (λ_{ex} = 275 nm) with a) 4-NP and b) Nit at concentration range 0-0.17 mM.

Fluorescence titrations of ZnGel in DMF in presence of different metal ions

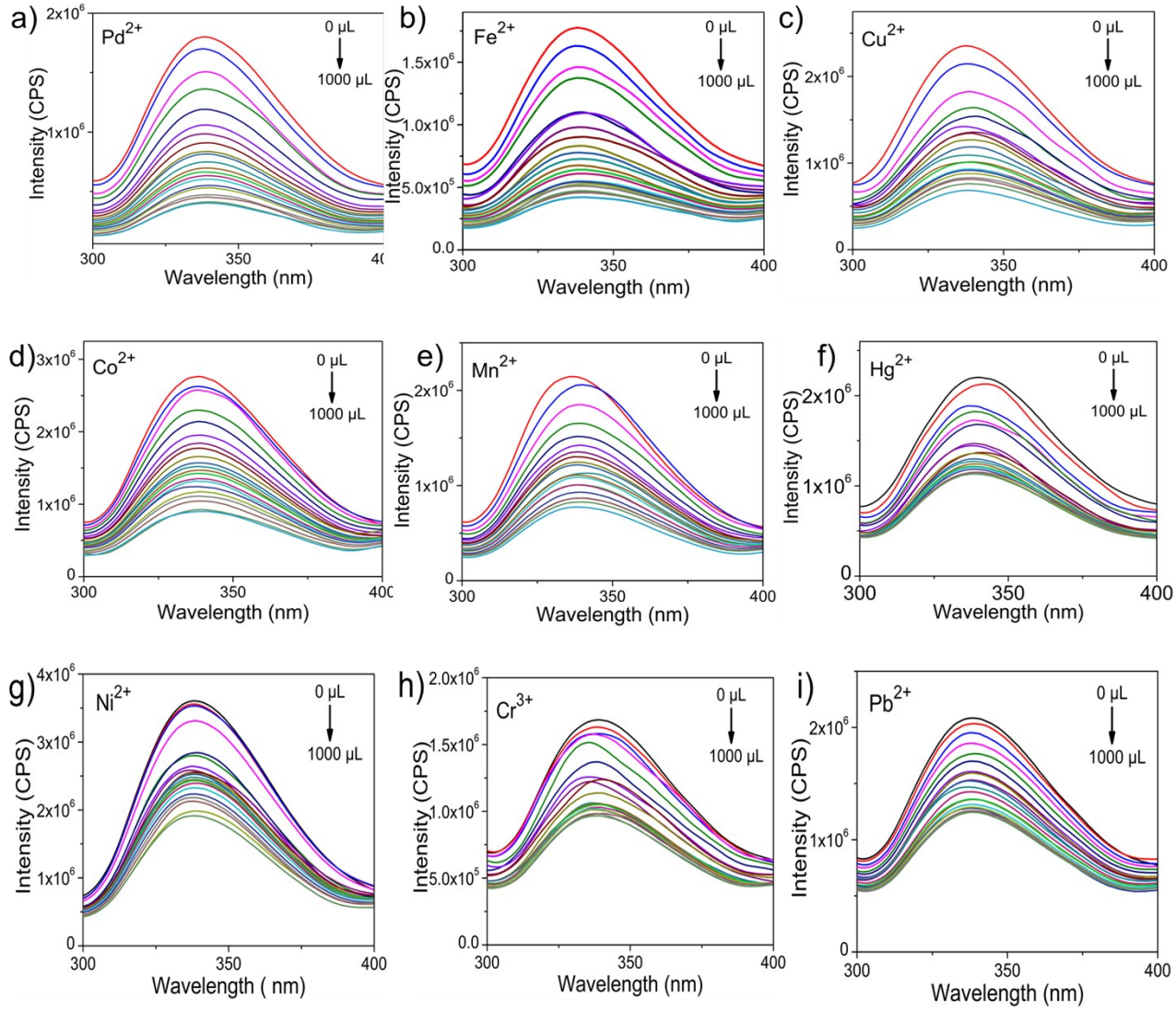

Figure S22. Fluorescence titrations of **ZnGel** in DMF (λ_{ex} = 275 nm) with a) Pd^{2+}, b) Fe^{2+}, c) Cu^{2+}, d) Co^{2+}, e) Mn^{2+}, f) Hg^{2+}, g) Ni^{2+}, h) Cr^{3+} and i) Pb^{2+} respectively.

Stern-Volver plots of ZnGel in DMF in presence of different metal ions

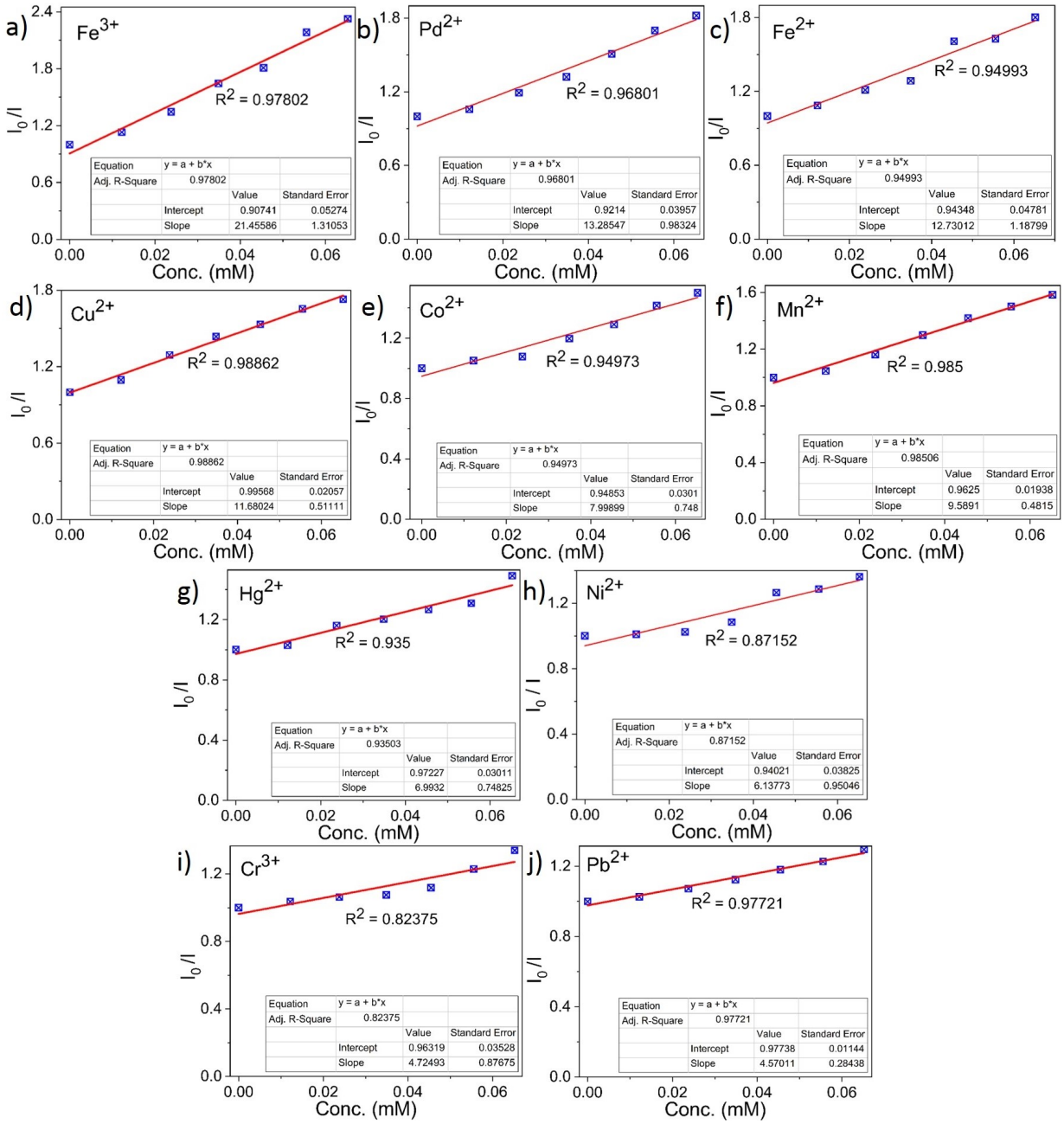

Figure S23. Stern-Volmer plots of **ZnGel** in DMF (λ_{ex} = 275 nm) with a) Fe^{3+}, b) Pd^{2+}, c) Fe^{2+}, d) Cu^{2+}, e) Co^{2+}, f) Mn^{2+}, g) Hg^{2+}, h) Ni^{2+}, i) Cr^{3+} and j) Pb^{2+} respectively.

Intensity of ZnGel vs concentration of the metal ions plot

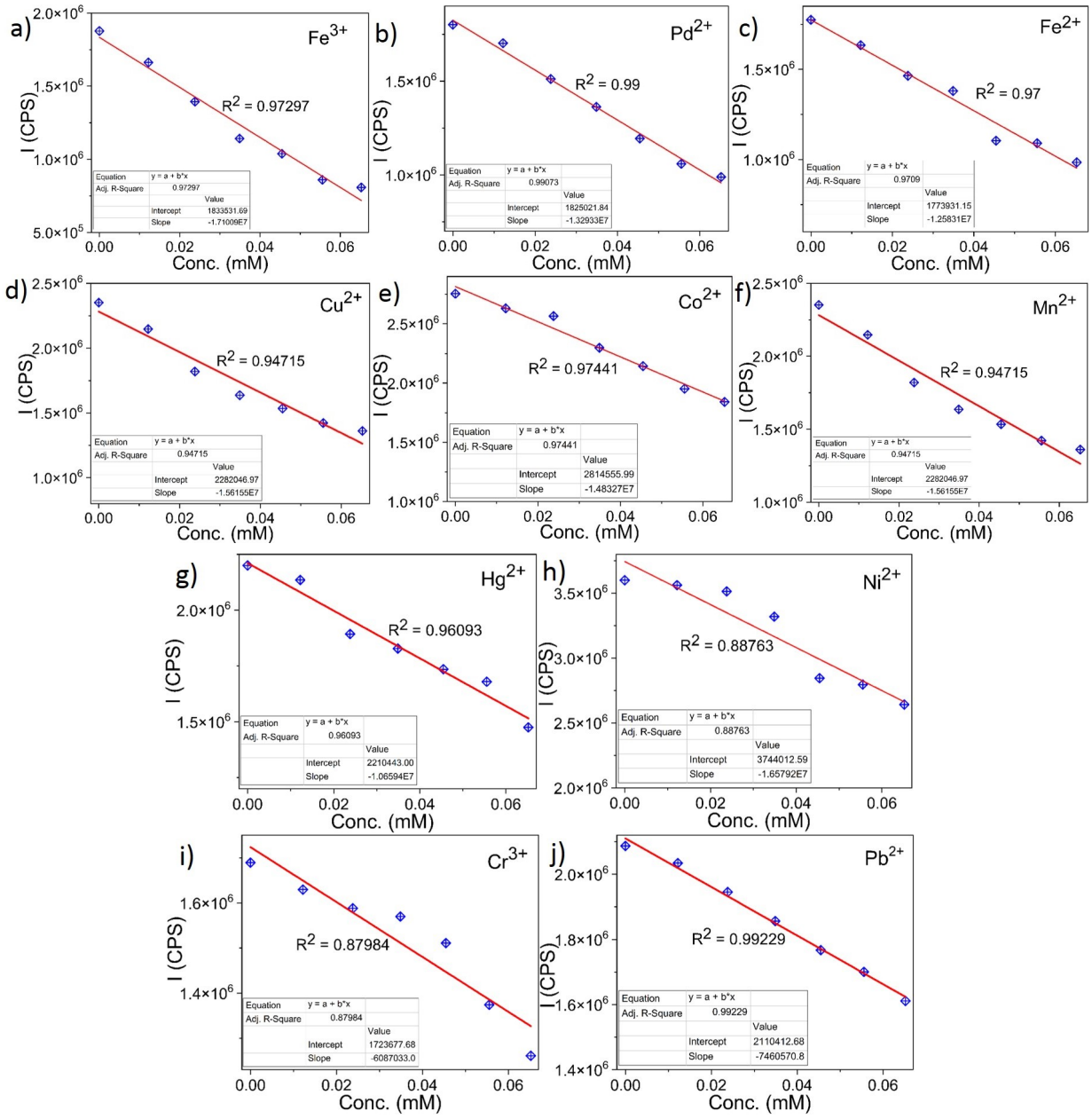

Figure S24. C vs I plots of **ZnGel** in DMF (λ_{ex} = 275 nm) with a) Fe^{3+}, b) Pd^{2+}, c) Fe^{2+}, d) Cu^{2+}, e) Co^{2+}, f) Mn^{2+}, g) Hg^{2+}, h) Ni^{2+}, i) Cr^{3+} and j) Pb^{2+} respectively.

Doping/ Uptake-study of NDs, NACs and metal ions into the gel: Naked-eye sensing in gel-to-gel states

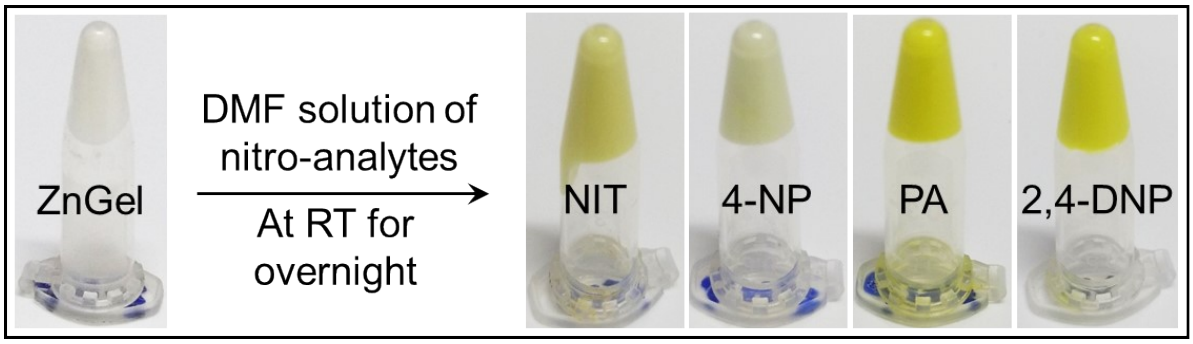

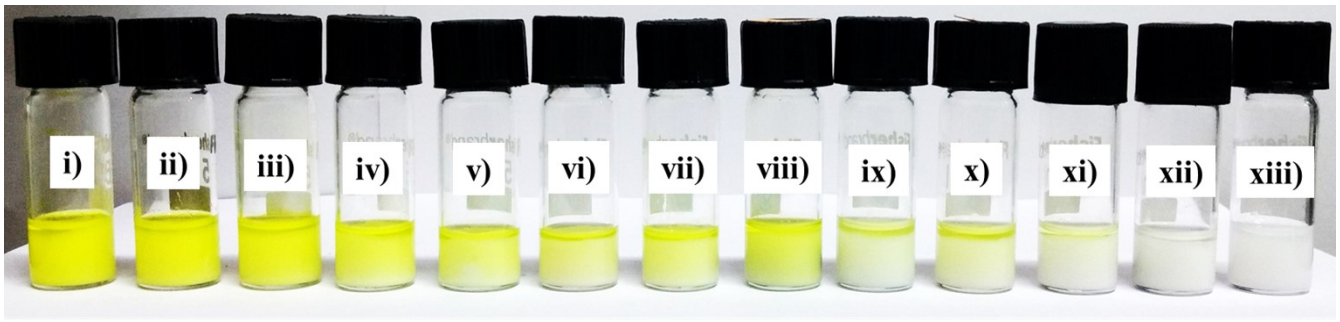

Figure S25. Top Panel shows the visual changes in **ZnGel** respectively upon nitro-analyte uptake. **Bottom Panel**: Naked-eye response of the metallogel when incubated with ethanolic solution of picric acid having varying concentrations [i) 5×10^{-2} M, ii) 2.5×10^{-2} M, iii) 1.0×10^{-2} M, iv) 5×10^{-3} M, v) 2.5×10^{-3} M, vi) 1.0×10^{-3} M, vii) 5×10^{-4} M, viii) 2.5×10^{-4} M, ix) 1.0×10^{-4} M, x) 5×10^{-5} M, xi) 1.0×10^{-5} M, xii) 1.0×10^{-6} M and xiii) 1.0×10^{-7} M respectively]. Naked-eye detection is possible only up to 10 μM solution.

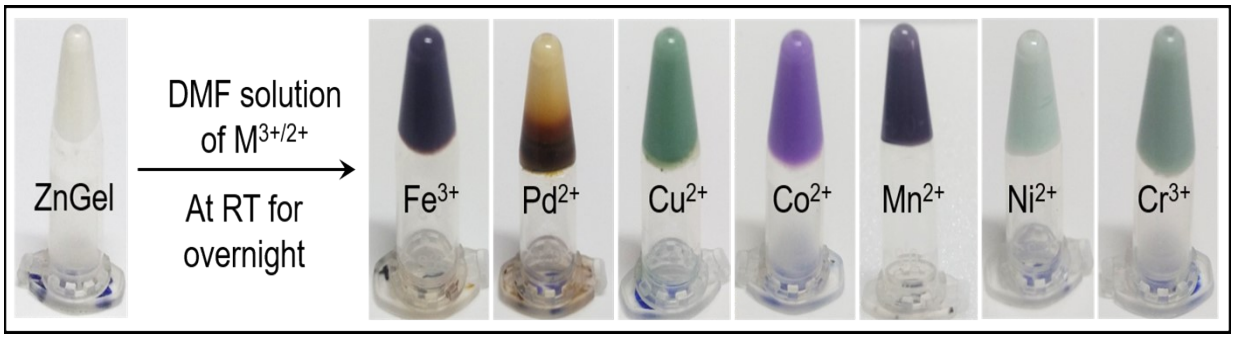

Figure S26. Shows the visual changes in **ZnGel** respectively upon metal uptake.

Spectral overlap between the emission spectrum of ZnGel with the absorption spectra of different NACs

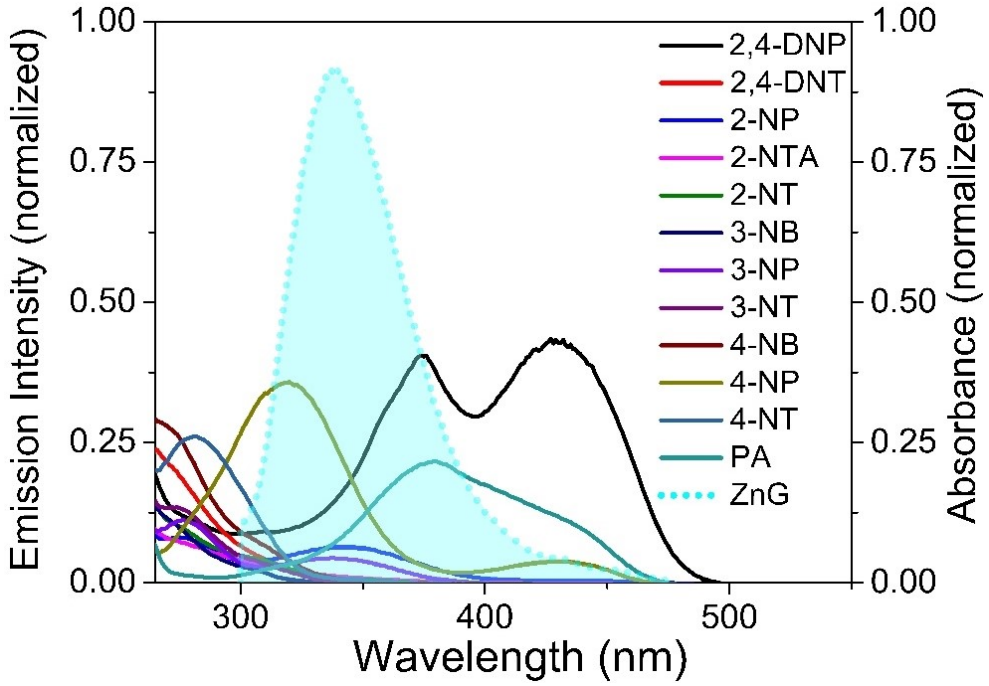

Figure S27. Spectral overlap between the emission spectrum of **ZnGel** (here ZnG) with the absorption spectra of respective NACs.

DFT optimized structures of the nitro analytes

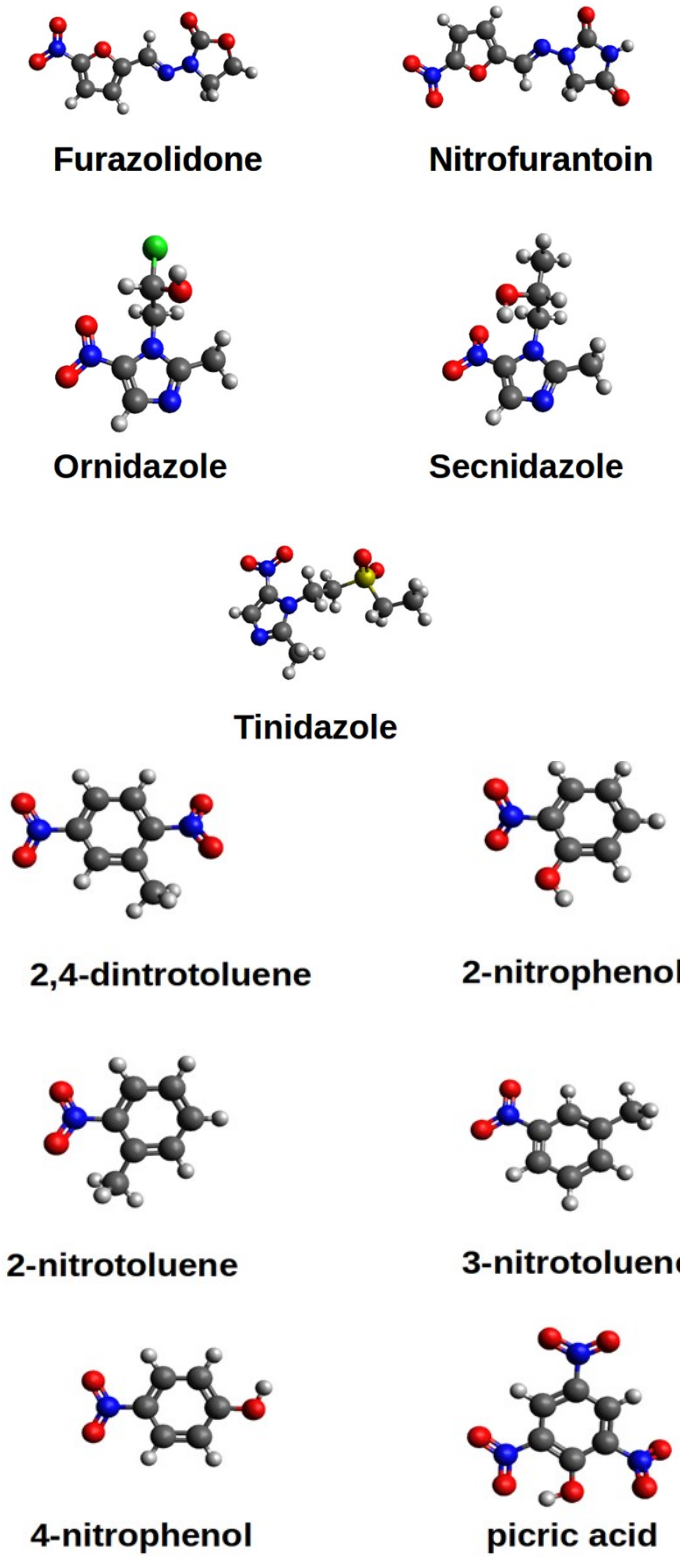

Figure S28. DFT-optimized structures of the antibiotics and nitro aromatics.

Frontier orbital energy levels from DFT

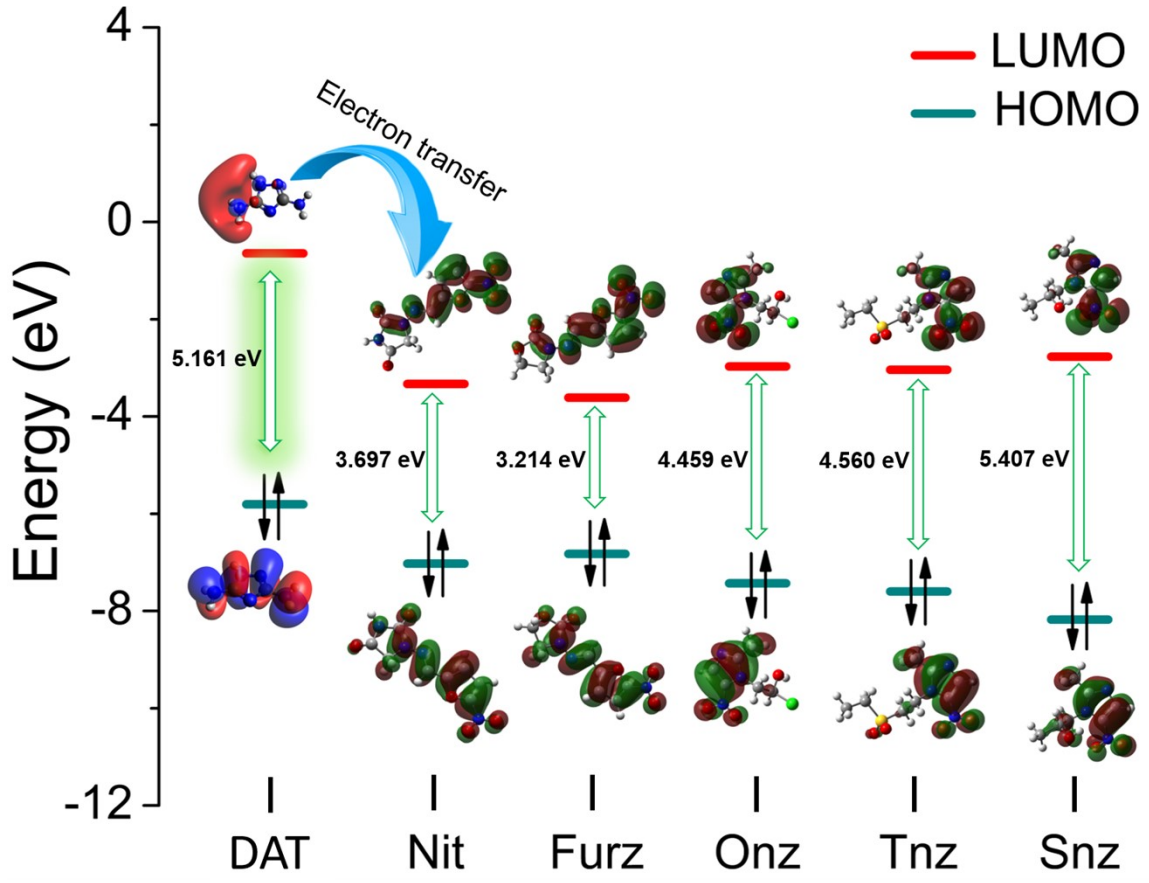

Figure S29. HOMO-LUMO energy (eV) plot for the antibiotics.

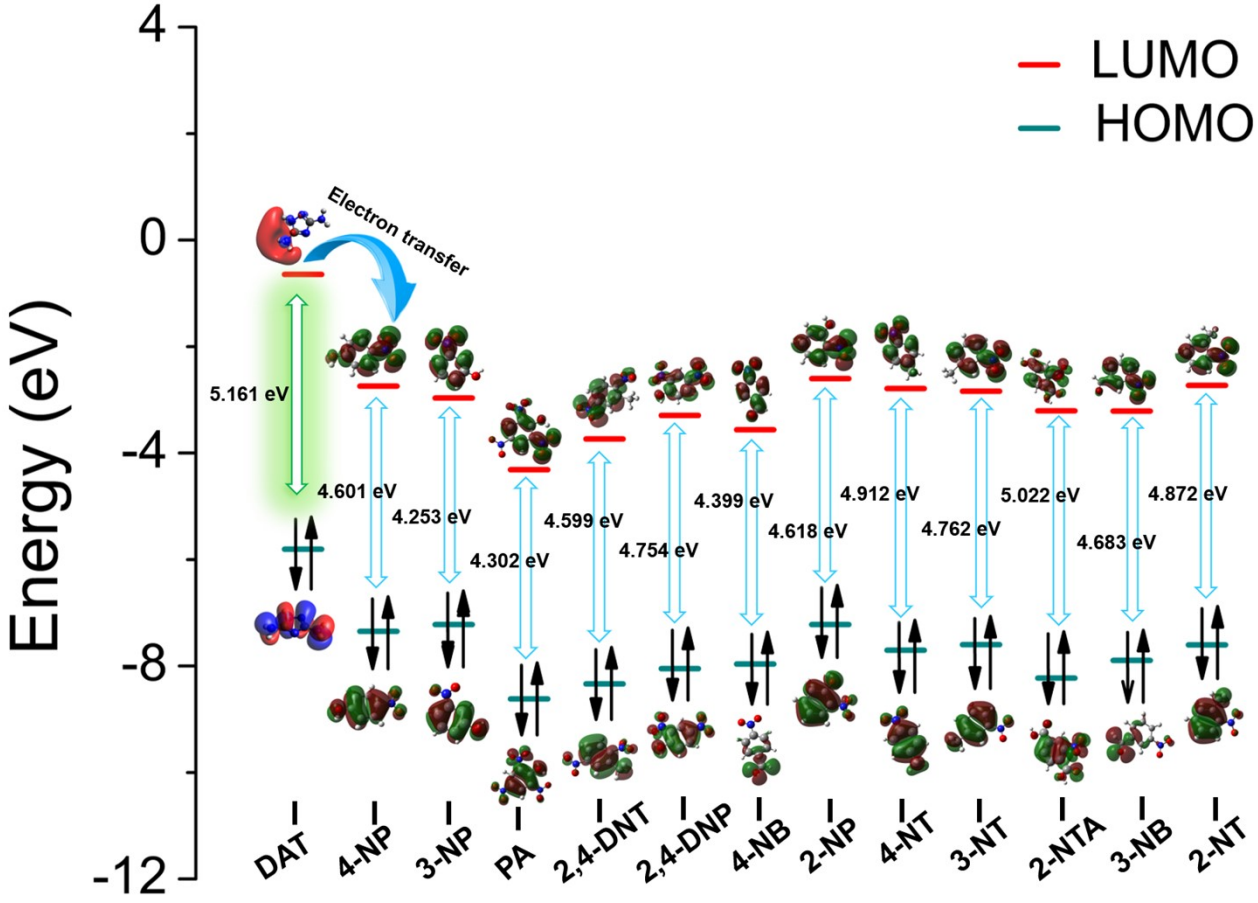

Figure S30. HOMO-LUMO energy (eV) plot for the nitroaromatics.

Anti-interference experiments

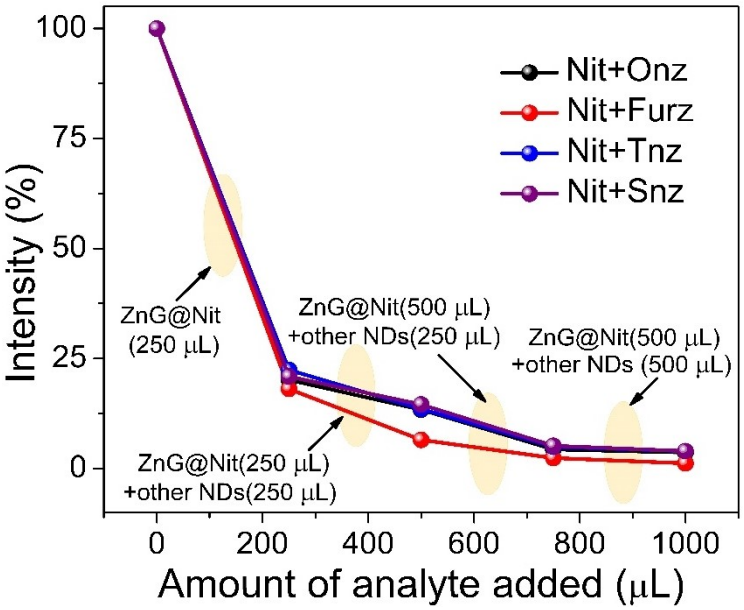

Figure S31. Quenching of the PL efficiency of **ZnGel** (here ZnG) by Nit, in presence of other competing nitro antibiotics.

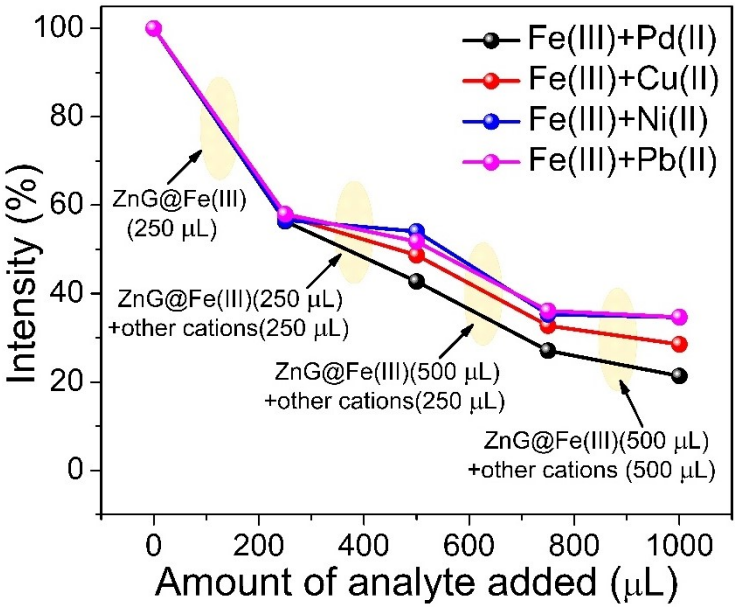

Figure S32. Quenching of the PL efficiency of **ZnGel** (here ZnG) by Fe(III), in presence of other competing metal ions.

Rapid detection of analytes

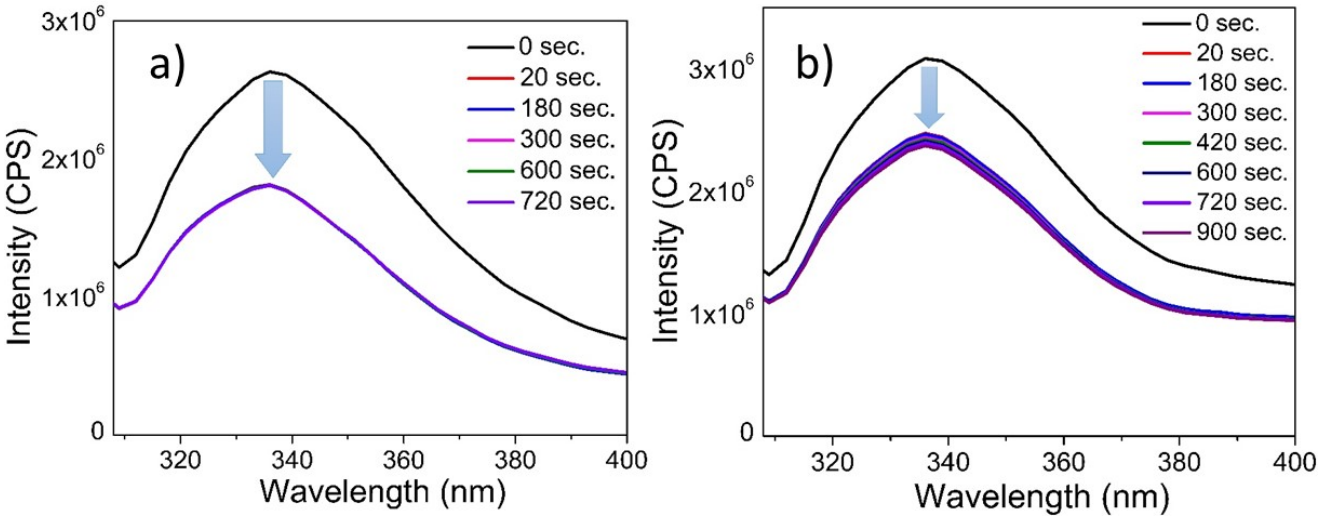

Figure S33. Rapid response of **ZnGel** within the first 20 seconds, in the detection of a) nitrofurantoin and b) furazolidone.

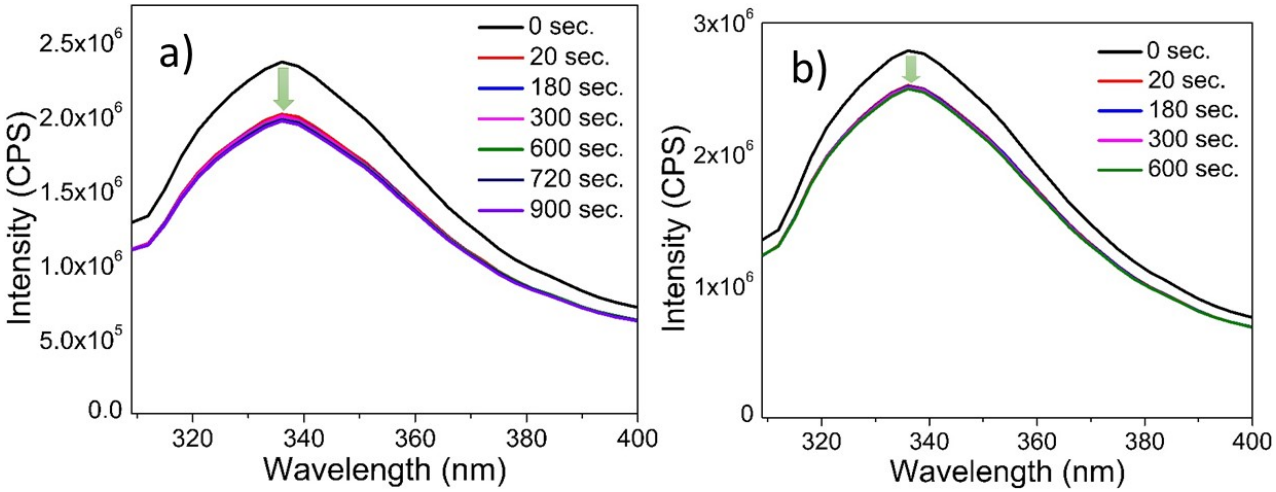

Figure S34. Rapid response of **ZnGel** within the first 20 seconds, in the detection of metal salts a) Fe^{3+} and b) Pd^{2+}.

Calculation for the Limit of Detection for respective analytes using ZnGel as the probe

Table S1. Calculation of standard deviation of fluorescence intensity and limit of detection for **ZnGel** towards nitrofurantoin.

Blank Readings (**ZnGel**)	Fluorescence Intensity (CPS)
Reading 1	1870240.76
Reading 2	1965361.88
Reading 3	1912174.20
Reading 4	2269097.03
Reading 5	2018221.20
Standard Deviation (σ)	156723.899
Slope from Curve (K)	2.4181×10^7 mM^{-1}
Detection Limit (3σ/K)	**0.0194 mM**
Limit of Detection (LOD)	**4.62 ppm**

Table S2. Calculation of standard deviation of fluorescence intensity and limit of detection for **ZnGel** towards furazolidone.

Blank Readings (**ZnGel**)	Fluorescence Intensity (CPS)
Reading 1	1870240.76
Reading 2	1965361.88
Reading 3	1912174.20
Reading 4	2269097.03
Reading 5	2018221.20
Standard Deviation (σ)	156723.899
Slope from Curve (K)	2.34902×10^7 mM^{-1}
Detection Limit (3σ/K)	**0.02 mM**
Limit of Detection (LOD)	**4.50 ppm**

Table S3. Calculation of standard deviation of fluorescence intensity and limit of detection for **ZnGel** towards Fe^{3+}.

Blank Readings (**ZnGel**)	Fluorescence Intensity (CPS)
Reading 1	1686257.90
Reading 2	1776526.68
Reading 3	1879131.23
Reading 4	2084091.26
Reading 5	1801332.14
Standard Deviation (σ)	150102.47
Slope from Curve (K)	1.71009×10^7 mM^{-1}
Detection Limit (3σ/K)	**0.0263 mM**
Limit of Detection (LOD)	**6.13 ppm**

Table S4. Calculation of standard deviation of fluorescence intensity and limit of detection for **ZnGel** towards 4-NP.

Blank Readings (**ZnGel**)	Fluorescence Intensity (CPS)
Reading 1	1686257.90
Reading 2	1776526.68
Reading 3	1879131.23
Reading 4	2084091.26
Reading 5	1801332.14
Standard Deviation (σ)	150102.47
Slope from Curve (K)	1.49625×10^{7} mM^{-1}
Detection Limit (3σ/K)	**0.0301 mM**
Limit of Detection (LOD)	**4.18 ppm**

Table S5. Comparative Study with reported sensor materials for Nitrofurantoin

Sl. No.	**Name of the analytes**	**Sensor (probe) material used**	**Limit of Detection (LOD)**	**References**
1.	Nitrofurantoin	Zn(II)-based metallogel	4.62 ppm (0.0194 mM)	*This work*
2.	Nitrofurantoin	Copper nanoclusters	0.73 µM	6
3.	Nitrofurantoin	Luminescent drug-based carbon nanodots	1.4 µM	7
4.	Nitrofurantoin	Zn(II)-Coordination Polymer	-	8
5.	Nitrofurantoin	bismuth titanate enclosed carbon nanofiber	0.005 µM	9
6.	Nitrofurantoin	Amide based low-molecular weight gelator (LMWG)	150 nM	10

Table S6. Comparative Study with reported sensor materials for Furazolidone

Sl. No.	**Name of the analytes**	**Sensor (probe) material used**	**Limit of Detection (LOD)**	**References**
1.	Furazolidone	Zn(II)-based metallogel	4.50 ppm (0.02 mM)	*This work*
2.	Furazolidone	*Pyoverdine*	0.5 mM	11
3.	Furazolidone	Carbon dots	0.096 µM	12
4.	Furazolidone	silica nanoparticles (type 1, FMSN-1)	4.46×10^{-6} M	13
5.	Furazolidone	glutathione-templated copper nanoclusters	0.012 µM	14
6.	Furazolidone	Pyoverdine	0.5 µM	15

Table S7. Comparative Study with reported sensor materials for Fe^{3+} ion

Sl. No.	Name of the analytes	Sensor (probe) material used	Limit of Detection (LOD)	References
1.	Fe^{3+}	Zn(II)-based metallogel	6.13 ppm (0.0263 mM)	*This work*
2.	Fe^{3+}	$[Zn_3(bpg)_{1.5}(azdc)_3]\cdot(DMF)_{5.9}\cdot(H_2O)_{1.05}$	1.71 ppm (1.29 μM)	16
3.	Fe^{3+}	[Cd(**L1**)(oba)]·DMF	103 ppb	17
4.	Fe^{3+}	$[Zn_2(\mathbf{L1})_2(HBPT)_2]\cdot H_2O$	72 ppb	17
5.	Fe^{3+}	$[Zr_6O_4(OH)_4(C_8H_2O_4S_2)_6]\cdot DMF\cdot 18H_2O$	1.26×10^{-6} M	18
6.	Fe^{3+}	Cd(PAM)(4-bpdb)1.5]·DMF	0.3 μM	19
7.	Fe^{3+}	$Zn_2(TPOM)(NDC)_2]\cdot 3.5H_2O$	2 μM	20
8.	Fe^{3+}	$[Zn_5(hfipbb)_4(trz)_2(H_2O)_2]$	~0.20 $mmol\cdot L^{-1}$	21
9.	Fe^{3+}	Zn-based coordination compound $[Zn(OOCC_6F_5)(H_2O)(C_{12}H_8N_2)_2]$ $(OOCC_6F_5)$	0.240 μM	22
10.	Fe^{3+}	Carbon dots and quantum dots-based nanohybrid	0.26 μM	23
10.	Fe^{3+}	imidazole-based chemosensor	0.27 μM	24
12.	Fe^{3+}	Rhodamine based chemosensor	9.2×10^{-8} M (5.5 μg/L)	25
13.	Fe^{3+}	4-(diethylamino)-2-(hydroxy)-phenyl imine functionalized naphthalimide	3.95×10^{-8} M	26
14.	Fe^{3+}	Fe_3O_4@ZnO	3 nmol L^{-1}	27
15.	Fe^{3+}	Au nanoclusters functionalized with 3,4-Dihydroxyphenylalanine	3.5 μM	28
16.	Fe^{3+}	Au nanorods	1.79 μM	29
17.	Fe^{3+}	Anionic Zn-MOF based on H_6TDPAT (2,4,6-tris(3,5-dicarboxylphenylamino)-1,3,5-triazine)	0.0233 mM	30
18.	Fe^{3+}	bi-component supramolecular polymer hydrogel based on tripodal gelators	5.33×10^{-9} M and 1.61×10^{-8} M	31
19.	Fe^{3+}	pillar[5]arene-based supramolecular organic framework gel	0.102 nM	32

References

1. Stewart, J. J. P. Optimization of parameters for semiempirical methods I. Method. *J. Comput. Chem*. **1989**, *10*(2), 209–220. DOI: 10.1002/jcc.540100208
2. Frisch, M.; Trucks, G.; Schlegel, H.; Scuseria, G.; Robb, M.; Cheeseman, J. et al. Gaussian 09, Revision B.01. Gaussian 09, Revision B01, Gaussian, Inc, Wallingford CT. **2009**.
3. Lee, C.; Yang, W.; Parr, R. G. Development of the Colle-Salvetti correlation-energy formula into a functional of the electron density. *Phys. Rev. B Condens. Matter*. **1988**, *37*(2), 785–789. DOI: 10.1103/PhysRevB.37.785
4. Becke, A. D. Density-functional exchange-energy approximation with correct asymptotic behavior. *Phys Rev A*. **1988**, *38*, 3098–3100. DOI: 10.1103/PhysRevA.38.3098
5. Ditchfield, R.; Hehre, W. J.; Pople, J. A. Self-Consistent Molecular-Orbital Methods. IX. An Extended Gaussian-Type Basis for Molecular-Orbital Studies of Organic Molecules. *J. Chem. Phys*. **1971**, *54*, 724–728. DOI: 10.1063/1.1674902
6. Cai, Z.; Pang, S.; Wu, L.; Hao, E.; Rong, J. *Spectrochim. Acta A Mol. Biomol. Spectrosc.* **2021**, *255*, 119737. DOI: 10.1016/j.saa.2021.119737
7. Al-Hashimi, B. R.; Omer, K. M.; Rahman, H. S.; Othman, H. H. *Spectrochim. Acta A Mol. Biomol. Spectrosc.* **2021**, *244*, 118835. DOI: 10.1016/j.saa.2020.118835
8. Liu, M.; Chi, Y. *J. Fluoresc.* **2020**, *30*(5), 1035-1042. DOI: 10.1007/s10895-020-02575-2
9. Nataraj, N.; Chen, S-M. *J. Electroanal. Chem.* **2021**, *887*, 115152. DOI: 10.1016/j.jelechem.2021.115152
10. Goyal, H.; Pachisia, S.; Gupta, R. *Cryst. Growth Des.* **2020**, *20*(9), 6117–6128. DOI: 10.1021/acs.cgd.0c00820
11. Yin, K.; Zhang, W.; Chen, L. *Biosens. Bioelectron.* **2014**, *51*, 90–96. DOI: 10.1016/j.bios.2013.07.038
12. Zhang, S.; Wang, Z.; Pang, Y.; Jing, Z.; Li, Z.; Peng, F.; Zhao, Y.; Guo, Y. *Spectrochim. Acta A Mol. Biomol. Spectrosc.* **2021**, *260*, 119969. DOI: 10.1016/j.saa.2021.119969
13. Wang, C.; Li, Q.; Wang, B.; Li, D.; Yu, J. *Inorg. Chem. Front.* **2018**, *5*, 2183-2188. DOI: 10.1039/c8qi00622a
14. Cai, Z.; Wu, L.; Qi, K.; Deng, C.; Zhang, C. *Spectrochim. Acta A Mol. Biomol. Spectrosc.* **2021**, *247*, 119145. DOI: 10.1016/j.saa.2020.119145
15. Yin, K. *Springer Theses* **2019**, 25–35. DOI: 10.1007/978-981-13-6488-4_3
16. Goswami, R.; Mandal, S. C.; Pathak, B.; Neogi, S. *ACS Appl. Mater. Interfaces* **2019**, *11*, 9042−9053. DOI: 10.1021/acsami.8b20013
17. Liu, Z.; Chen, K.; Zhao, Y.; Kang, Y.; Liu, X.; Lu, Q.; Azam, M.; Al-Resayes, S. I.; Sun, W. *Cryst. Growth Des*. **2018**, *18*, 1136−1146. DOI: 10.1021/acs.cgd.7b01572

18. Dalapati, R.; Kökçam-Demir, U.; Janiak, C.; Biswas, S. *Dalton Trans*. **2018**, *47*, 1159–1170. DOI: 10.1039/C7DT04130F
19. Lv, R.; Chen, Z.; Fu, X.; Yang, B.; Li, H.; Su, J.; Gu, W.; Liu, X. *J. Solid State Chem.* **2018**, *259*, 67–72. DOI: 10.1016/j.jssc.2017.12.033
20. Lv, R.; Li, H.; Su, J.; Fu, X.; Yang, B.; Gu, B.; Liu, X. *Inorg. Chem*. **2017**, *56*, 12348−12356. DOI: 10.1021/acs.inorgchem.7b01822
21. Hou, B.; Tian, D.; Liu, J.; Dong, L.; Li, S.; Li, D.; Lan, Y. *Inorg. Chem*. **2016**, *55*, 10580−10586. DOI: 10.1021/acs.inorgchem.6b01809
22. Han, L.-J.; Kong, Y.-J.; Xu, Y.-Y.; Huang, M.-M. *Polyhedron* **2021**, *193*, 114868. DOI: 10.1016/j.poly.2020.114868
23. Zhang, L.; Chang, J.; Su, R.; Huang, R.; Qi, W.; He, Z. *Chem. Eng. Trans*. **2018**, *70*, 2065-2070. DOI: 10.3303/CET1870345
24. Jo, T. G.; Bok, K. H.; Han, J.; Lim, M. H.; Kim, C. *Dyes Pigm.* **2017**, *139*, 136–147. DOI: 10.1016/j.dyepig.2016.11.052
25. Lan, T.; Wang, F.-H.; Xi, X.-J.; Cheng, C.-W.; Lei, W.; Xia, M.-Z.; Wang, F.-Y. *Anal. Sci.* **2016**, *32*(11), 1223–1229. DOI: 10.2116/analsci.32.1223
26. Zhang, Y.-M.; Han, B.; Mao, P.; Chen, J.; Yao, H.; Wei, T.-B.; Lin, Q. *Can. J. Chem.* **2019**, *97*(8), 597-602. DOI: 10.1139/cjc-2018-0138
27. Li, J.; Wang, Q.; Guo, Z.; Ma, H.; Zhang, Y.; Wang, B.; Bin, D.; Wei, Q. *Sci. Rep.* **2016**, *6*(1). DOI: 10.1038/srep23558
28. Ho, J-a. A.; Chang, H. C.; Su, W. T. *Anal. Chem.* **2012**, *84*(7), 3246–3253.
29. Thatai, S.; Khurana, P.; Prasad, S.; Kumar, D. *Microchem J.* **2014**, *113*, 77–82.
30. Chen, C.-H.; Wang, X.-S.; Li, L.; Huang, Y.-B.; Cao, R. *Dalton Trans.* **2018**, *47*(10), 3452–3458. DOI: 10.1039/c8dt00088c
31. Zhao, Q.; Dai, X-Y.; Yao, H.; Zhang, Y-M.; Qu, W-J.; Lin, Q.; Wei, T. B. *Dyes Pigm.* **2021**, *184*, 108875. DOI: 10.1016/j.dyepig.2020.108875
32. Zhang, Y.-M.; He, J.-X.; Zhu, W.; Li, Y.-F.; Fang, H.; Yao, H., Wei, T.B.; Lin, Q. *Mater. Sci. Eng. C* **2019**, *100*, 62–69. DOI: 10.1016/j.msec.2019.02.094